mainly Ce-, Pr-, and Tb-based materials, in which 4+ and 3+ oxidation states are accessible. Although no visible luminescence was observed in any of these materials, none of them allowed the $M^{4+}$ cation to exist in a coordination environment where terminal M-O bonds exist. Scheelite as well as other minerals and synthetic materials containing high–oxidation state metal ions also luminesce by charge-transfer type mechanisms (*7*).

To ascertain if there were other luminescent phases within the $M_2CeO_4$ (M = Ba, Ca, and Mg) phase space, a triangular library was prepared with the $M_2CeO_4$ compositions at each corner. This library was prepared by robotically dispensed sol-gel precursors and followed by heating to 900°C. Under 254-nm excitation (Fig. 3), the Sr-containing region has the brightest emission, and there is no appreciable luminosity from the Ba and Mg regions. Once the stable sol-gel precursors were synthesized, deposition of the library took ~15 to 20 min. Powder x-ray diffraction of the individual elements confirmed that no additional phases isotypic to $Sr_2CeO_4$ exist on this library.

Although combinatorial methods might initially appear to be limited to substitutional variants of existing materials, this work shows that unexpected structures can be identified. After isolation, structural and spectroscopic studies showed that $Sr_2CeO_4$ possesses a phosphor structure type that emits light not by the usual mechanism originating from within the electronic states of a paramagnetic rare-earth site, but rather from a charge-transfer mechanism. The identification of a material displaying a property (luminescence) that arises through an unusual mechanism illustrates the possibilities that the combinatorial approach can open in materials science.

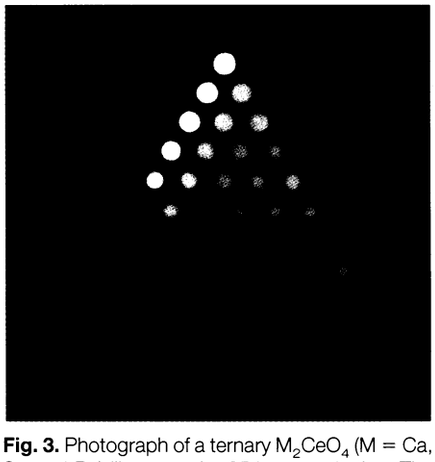

**Fig. 3.** Photograph of a ternary $M_2CeO_4$ (M = Ca, Sr, and Ba) library under 254-nm excitation. The Ce concentration in each element is constant, and the M gradient decreases linearly from the corner of the pure $M_2CeO_4$ composition in a direction along the bisector of the opposite edge. Element map: Sr, top; Ba, lower left; and Ca, lower right.

## REFERENCES AND NOTES


1. X.-D. Xiang *et al.*, *Science* **268**, 1738 (1995).
2. G. Briceño, H. Chang, X. Sun, P. G. Schultz, X.-D. Xiang, *ibid.* **270**, 273 (1995).
3. E. Danielson *et al.*, *Nature* **389**, 944 (1997).
4. M. D. Mastromonaco, I. Barbariol, A. Cocco, *Ann. Chim. (Rome)* **59**, 465 (1969).
5. Step-scanned x-ray powder diffraction data for the sample were collected with the use of a 9-kW rotating anode generator equipped with a copper target and graphite monochromator. Data were collected in the 2θ range from 15° to 110° with a step size of 0.01° and a count time of 6 s per step. The powder pattern was indexed by standard methods. Space group *Pbam*, $a$ = 6.11897(9) Å, $b$ = 10.3495(2) Å, and $c$ = 3.5970(1) Å. The intensities were extracted using the program EXTRA [A. Altomore *et al.*, *J. Appl. Crystallogr.* **28**, 842, (1995)], and the structure was solved ab initio using SIRPOW [A. Altomore *et al.*, *Acta Crystallogr. A* **47**, 744 (1991)]. Full-pattern Rietveld refinement was carried out using the program GSAS. Final refinement converged with $R_{wp}$ = 0.081, $R_p$ = 0.059, and $R_F$ = 0.026 for 172 independent observations.
6. H. E. Hoeffdraad, *J. Inorg. Nucl. Chem.* **37**, 1917 (1975).
7. G. Blasse and B. C. Grabmaier, *Luminescent Materials* (Springer-Verlag, Berlin, 1994); J. L. Ouweltjes, "Luminescence and Phosphors," *Modern Materials* **5**, 161 (1965).


8. This work would not have been possible without technical assistance from G. Wallace-Freedman, Y. Wang, and J. Wu. The authors also acknowledge helpful advice from J. McCusker and S. Jacobsen. We are grateful for the ESR measurements performed by B. Warren (Sandia National Laboratory). The experimental details for the preparation and processing of the focus and discovery libraries as well as the crystallographic data are available as supplementary material at www.sciencemag.org/feature/data/975265.shl

29 September 1997; accepted 23 December 1997


# Frictional Melting During the Rupture of the 1994 Bolivian Earthquake

Hiroo Kanamori, Don L. Anderson, Thomas H. Heaton

**The source parameters of the 1994 Bolivian earthquake (magnitude $M_w$ = 8.3) suggest that the maximum seismic efficiency η was 0.036 and the minimum frictional stress was 550 bars. Thus, the source process was dissipative, which is consistent with the observed slow rupture speed, only 20% of the local *S*-wave velocity. The amount of nonradiated energy produced during the Bolivian rupture was comparable to, or larger than, the thermal energy of the 1980 Mount St. Helens eruption and was sufficient to have melted a layer as thick as 31 centimeters. Once rupture was initiated, melting could occur, which reduces friction and promotes fault slip.**

The possibility of frictional melting during faulting has been suggested by several investigators (*1*–*4*). McKenzie and Brune (*2*) quantitatively investigated this problem as a one-dimensional heat conduction problem. They assumed that the fault surface is simultaneously heated during slippage (that is, infinite rupture speed) over a finite time. The temperature was determined mainly by generation of heat (the integrated product of slip and frictional stress) and diffusion of heat (controlled by duration of the heating event and thermal diffusivity). The duration of heating was determined by the driving stress on the fault. If the driving stress was lower, the heating process was slower, allowing heat to diffuse over a larger distance away from the fault; this case results in less temperature rise. They concluded that if the frictional and driving stresses are of the order of 1 kbar, melting could occur for fault slips as small as 1 mm. Richards (*4*) solved elastodynamic equations for a propagating elliptical crack and estimated the frictional heating rate behind a rupture front. He showed that if the driving stress is 100 bars and the fault particle velocity is 10 cm/s at the time of rupture nucleation, a temperature rise of about 1000°C can occur within a few seconds at a point halfway between the rupture front and the point of nucleation. These studies indicate that frictional melting can occur if the stresses involved in faulting are sufficiently high. Despite these studies, frictional melting is not generally regarded as an important process during earthquake faulting because of uncertainties in the stress levels—especially the magnitude of frictional stresses—associated with earthquakes and uncertainties in the detailed fault-zone structures. Sibson (*3*) noted that production of pseudotachylyte (glassy material presumably formed by frictional melting) should take place during faulting, but very few faults contain pseudo-tachylytes.

The 9 June 1994 $M_w$ = 8.3 Bolivian event (13.86°S, 67.54°W; depth = 637 km) was a large deep-focus earthquake (source parameters shown in Table 1). Although the results obtained by different studies vary in detail, the values of most source parameters

Seismological Laboratory, California Institute of Technology, Pasadena, CA 91125, USA.

agree. The seismic moment was $M_0 = 3 \times 10^{21}$ N·m (the median of the values listed in Table 1). The main shock consisted of several discrete events, here called subevents. The rupture area $S$ was determined from the spatial spreads of all of the subevents, and the estimates range from 1000 to 2500 km$^2$; the range in $S$ is mainly due to the difference in how the outer boundary of the subevent distribution was delineated. Here we used the estimate obtained by Kikuchi and Kanamori (*5*), $S = 40$ km $\times$ 40 km, which is close to the middle of the range of $S$ listed in Table 1. If we use only the area where the displacement was larger than 10 m, $S$ can be smaller (15 km $\times$ 30 km) (*6*). The spatial extent of the aftershock area was about 50 km (*7*), the same order as the rupture dimension estimated from waveform analysis. The source duration was about $\tau = 40$ s. The variation of the rupture speed $V$ reflects the different estimates of speed for different subevent pairs. Because the details of the rupture pattern could not be determined, the rupture speed was defined by the ratio of the distance between the subevents to the time difference between them. If we define the average rupture speed by the ratio of the total rupture length (about 40 km) to the rupture time (about 40 s), we obtain $V = 1$ km/s (Table 1). The estimated rupture speed of Chen (*8*) was high, 3 to 3.5 km/s, because he assumed that the subevents were distributed en echelon. Here we use $V = 1$ km/s, which corresponds to $V/\beta = 0.2$, where $\beta$ is the local $S$-wave velocity. From these parameters, the average fault offset is estimated to be $D = 15.6$ m, and the static stress drop $\Delta\sigma = 1.14$ kbar (*9*).

Another important source parameter is the radiated wave energy $E_R$. For shallow earthquakes, the determination of $E_R$ is uncertain because of complex wave propagation effects, but for deep-focus earthquakes, it can be determined relatively accurately. Winslow and Ruff (*10*) determined the radiated energy to be $E_R = 5.2 \times 10^{16}$ J by integrating the observed velocity records. This value is in good agreement with the previously reported values of $3.2 \times 10^{16}$ J (*11*) and $5.2 \times 10^{16}$ J (*12*).

Another notable feature of the Bolivian earthquake is the lack of any isotropic component (net volume change) over long periods. The isotropic component was insignificant, probably less than 2 to 4% of the double couple component (*5*, *13*, *14*). This value corresponds to a maximum volume change of $7.5 \times 10^7$ to $1.5 \times 10^8$ m$^3$, or a maximum fault-normal displacement of 12 to 24 cm.

The mechanism of deep-focus earthquake has been a matter of significant interest for many years. Because of the high pressure and temperature in the source region, the ordinary brittle failure is not likely to occur, and other mechanisms need to be invoked. Recently, Green and Burnley (*15*) and Kirby *et al.* (*16*) proposed transformational faulting as a plausible mechanism of deep-focus earthquakes. In this case, a phase transition triggers a rupture, but the main rupture occurs under the ambient shear stress. Also, rupture may nucleate on a weak zone established in a slab at the surface (*17*). Here we assume that some triggering mechanism initiated the Bolivia earthquake and address the question of what happened after the rupture began.

We first investigate the energy budget of the earthquake using only the quantities determined from seismic observations. The total potential-energy (strain energy plus gravitational energy) change $W$ can be written as (*18*)

$$W = (\sigma_0 + \sigma_1)DS/2 = \Delta\sigma DS/2 + \sigma_1 DS \quad (1)$$

where $\sigma_0$ and $\sigma_1$ are the initial and the final stresses on the fault plane, respectively, and $\Delta\sigma = \sigma_0 - \sigma_1$ is the static stress drop.

We define seismic efficiency $\eta$ by

$$\eta = (W - H_f)/W = E_R/W \quad (2)$$

where $H_f = \sigma_f SD$ is the frictional energy loss during faulting and $\sigma_f$ is the average frictional stress (*19*). Using the seismic moment $M_0 = \mu DS$, where $\mu$ is the rigidity, we can rewrite Eqs. 1 and 2 as $\eta = \mu(E_R/M_0)/(\sigma_1 + \Delta\sigma/2)$ and $\sigma_f = \mu(1 - \eta)(E_R/M_0)/\eta$.

For any physically reasonable stress release mechanism, $\sigma_1 \geq 0$. With this constraint, an upper bound for $\eta$ is given by

$$\eta_{max} = 2(E_R/M_0)\mu/\Delta\sigma \quad (3)$$

and a lower bound for $\sigma_f$ is given by

$$\sigma_{fmin} = (1 - \eta_{max})\Delta\sigma/2 \quad (4)$$

Using $E_R = 5.2 \times 10^{16}$ J (*10*–*12*), $\mu = 1.2$ Mbar, and $\Delta\sigma = 1.14$ kbar for the Bolivian earthquake, we obtain $\eta_{max} = 0.036$ and $\sigma_{fmin} = 550$ bars. From $\eta_{max}$, the lower bound of the nonradiated energy can be estimated as $H_{fmin} = W - E_R = E_R(1 - \eta_{max})/\eta_{max} = 1.4 \times 10^{18}$ J. For comparison, the total thermal energy released during the 1980 eruption of Mount St. Helens was about $10^{17}$ to $10^{18}$ J (*20*). Although this amount of heat does not significantly contribute to the global heat flow, it can influence the local thermal budget in subduction zones.

To estimate the overall thermal state in the focal region of the Bolivian earthquake, we consider the gross energy budget. If $H_f = \sigma_f SD$ is used to raise the temperature of a thin layer with thickness $\Delta d$, then the temperature increase $\Delta T$ over the volume $S\Delta d$ is given by

**Table 1.** Seismic moment $M_0$, rupture area $S$, source duration $\tau$, and rupture speed $V$ of the 1994 Bolivian earthquake as determined in various studies. The first moment is from the Harvard CMT solution.

| $M_0$ ($10^{21}$ N·m) | $S$ (km$^2$) | $\tau$ (s) | $V$ (km/s) | Ref. |
|---|---|---|---|---|
| 3.0 | | | | CMT |
| 3.0 | 40 × 40* | 40 | 1 | (*5*) |
| | 30 × 50 | 40 | 1 to 2.6 | (*17*) |
| 3.0 | | 46 | | (*14*) |
| 2.6 | 50 × 20† | 40 | 1 | (*34*) |
| 3.0 | 30 × 40† | 40 | 2 to 3‡ | (*35*) |
| 2.7 | | 50 | | (*36*) |
| | 30 × 50 | 40 | 1 to 2 | (*37*) |
| | | 40 | 3 to 3.5§ | (*8*) |
| 3.1 | | | | (*13*) |
| | 50 × 50 | 40 | | (*38*) |
| | 60 × 40‖ | | <2 | (*6*) |

*The area of main energy release is even smaller. †Area of main energy release. ‡Maximum rupture speed. §Rupture speed within en echelon subevents. The apparent rupture speed is 1 to 2 km/s. ‖Total area of rupture.

$$\Delta T = \sigma_f SD/C\Delta dS\rho \quad (5)$$

if no melting occurs. Here, $\rho$ is the density and $C$ is the heat capacity of the bulk rock. If melting occurs at temperature $T_m$, then $C\Delta T$ should be replaced by $C\Delta T_m + H + C_L(T - T_m)$, where $\Delta T_m$ (estimated as 600°C) is the temperature difference between the melting temperature and the ambient temperature in the slab (*21*), $C_L$ is the heat capacity for the liquid phase, and $H$ is the latent heat.

The thickness $\Delta d$ depends on how the heat is generated. If faulting occurs on an infinitesimally thin layer and heat diffuses out from there, $\Delta d$ will be of the order of the thermal penetration depth given by $\Delta d = (k\tau_d)^{1/2}$, where $\tau_d$ is the time scale of faulting and $k$ is the thermal diffusivity. If we choose $\tau_d = 10$ s as a characteristic local time scale of faulting for the Bolivian earthquake and $k = 1.35 \times 10^{-2}$ cm$^2$/s, then $\Delta d = 3.7$ mm (*22*). If faulting occurs on a distributed fault zone or in shear bands, $\Delta d$ can be larger. The resulting $\Delta T$ from Eq. 5 is shown in Fig. 1. In this computation, $H$ and the difference between $C$ and $C_L$ are ignored. We find that melting is likely to occur in some region near the fault zone if the slip zone is over a thickness of less than 31 cm (indicated by a dash-dot line at $\Delta T = 600$°C in Fig. 1). If the thermal penetration depth, $\Delta d = 3.7$ mm, is used, the local temperature rise is of the order of 52,000°C (indicated by a dash-dot line in Fig. 1). Figure 1 also compares the thermal energy density $H_f/\Delta dS\rho$ in the slip zone with the latent heat for melting, enthalpy for phase changes (because both are about the same on this scale, the range of $\Delta H$ for both is indicated by a dash-dot line at about

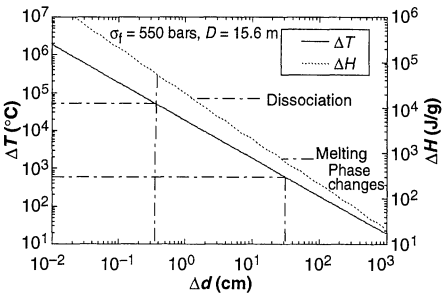


**Fig. 1.** Changes in temperature $\Delta T$ and enthalpy $\Delta H$ due to frictional heating as a function of the thickness of the slip zone $\Delta d$ ($\sigma_f$ = 550 bars and $D$ = 15.6 m). The density $\rho$ = 4 g/cm$^3$ for the depth of 637 km was used. The value of $C$ (1.14 J/g°C) used to calculate $\Delta T$, and the values of $\Delta H$ of melting, phase changes, and dissociation for $Mg_2SiO_4$ are taken from (*33*).

$\Delta H = 10^3$ J/g in Fig. 1), and dissociation (to elements) energy (indicated by a dash-dot line at about $\Delta H = 1.5 \times 10^4$ J/g in Fig. 1) of $Mg_2SiO_4$. If $\Delta d$ is less than a few millimeters, the available energy is sufficient to dissociate olivine to elements, and the material will be in a plasma-like state.

The thickness $\Delta d$ cannot be determined directly from seismological data, but weakening as a result of melting is likely to localize deformation on a thin zone, as is seen in pseudo-tachylytes. The small upper bound for the fault-normal displacement (*5*, *13*, *14*) also suggests a fairly simple dislocation source, and a large complex volumetric source is probably ruled out. Thus, $\Delta d$ as small as a few millimeters is plausible.

The slow rupture speed $V = 0.2\beta$ observed for the Bolivian earthquake is an independent observation that also suggests a dissipative rupture process. We discuss the implication of slow rupture speed using a simple crack theory. For Mode III cracks (antiplane shear crack), Kostrov (*23*) and Eshelby (*24*) showed that the energy flux to the crack tip (energy release rate) G is given by

$$G = g(V)G^* \quad (6)$$

where G* is the value of G computed for a quasi-static situation, and $g(V)$ is a universal function of $V$. Eshelby gives

$$g(V) = [(1 - V/\beta)/(1 + V/\beta)]^{1/2} \quad (7)$$

The equation of motion for rupture propagation can be obtained by equating G to $2\gamma$, where $\gamma$ is the surface energy. If $\gamma$ is independent of $V$, $V$ increases from 0 to $\beta$ as the crack length increases. Thus, the limiting rupture speed is $\beta$, which does not fit the characteristics of the Bolivian earthquake. However, if $\gamma$ increases with $V$ as a result of extensive plastic deformation near the crack tip, as experimentally demonstrated by Rosakis and Zehnder (*25*), $V$ can be significantly lower than the *S*-wave velocity.

In the above, frictional energy loss is not explicitly included, but during complex rupture propagation that involves large plastic deformations near the crack tip, distinction between surface energy and frictional energy is not obvious, especially if rupture propagation is slip-like (*26*). If we include frictional energy loss in the surface energy (*27*), then the efficiency $\eta$ is given by (G* − G)/G*, and using Eqs. 6 and 7, we obtain

$$\eta = 1 - g(V) = 1 - [(1 - V/\beta)/(1 + V/\beta)]^{1/2} \quad (8)$$

The exact relation between $\eta$ and $V/\beta$ depends on the specific crack model. If we use the energy-based crack model of Mott (*28*), the kinetic energy is proportional to $V^2$, and a relation

$$\eta = (V/\beta)^2 \quad (9)$$

is inferred instead of Eq. 8. Because $V/\beta$ = 0.2 for the Bolivian earthquake, we obtain $\eta$ = 0.18 and 0.04 from Eqs. 8 and 9, respectively. These values are consistent with the low $\eta_{max}$ estimated from seismic data for the Bolivian earthquake.

The molten layer can be very thin compared with the dimension of the fault plane. Then a question may be raised as to whether such a thin layer can have significant effects on sliding friction or not. In this connection, the effect of a thin molten layer on ski sliding, studied by Bowden and Hughes (*29*), provides an interesting analog of frictional melting during earthquake faulting. Bowden and Hughes experimentally demonstrated that a sliding ski can produce a thin film of water $10^{-2}$ cm thick or less and promote sliding with a low coefficient of friction $\mu_f = 0.03$.

It is unclear whether the Bolivian earthquake is fundamentally different from other deep-focus earthquakes. The ratio of $E_R$ to $M_0$ is generally low for most deep-focus earthquakes (*10*, *30*), suggesting a fairly dissipative rupture mechanism. However, because of the limited resolution of determination of source dimensions, the static stress drop and rupture speed for smaller deep-focus earthquakes are not well-determined. No evidence for slow rupture speed has been found for other deep-focus earthquakes, with the possible exception of the equally large 1970 Colombia earthquake ($M_w$ = 8.2), for which a rupture speed of 1 to 3.2 km/s was suggested (*31*). Because of these uncertainties, it is unclear whether melting plays a major role in other deep-focus earthquakes. Deep-focus earthquakes may be different from event to event (*32*). It is possible, however, that when the slip caused by some triggering mechanisms exceeds a threshold, melting occurs and promotes extensive sliding, which results in an exceptionally large deep-focus earthquake, such as the 1994 Bolivian event. As the quality and quantity of seismic data improve, the accuracy of source-parameter determinations will improve, so that we may eventually be able to resolve this question.

For most shallow earthquakes, the ratio of the rupture speed to the average crustal *S*-wave velocity is about 0.7 to 0.8. Considering the relatively low *S*-wave velocity near the fault zone and the various rupture modes in faulting, this ratio may represent an even higher ratio of rupture speed to the limiting velocity (for example, Rayleigh wave velocity) appropriate for a given rupture mode. If the mechanism of friction for shallow earthquakes is similar to that of the Bolivian earthquake, then the high ratio for shallow earthquakes may suggest a relatively nondissipative brittle rupture process, that is, faulting with low frictional stress. Resolution of this problem, however, requires further studies on the mechanism of friction during seismic rupture.

## REFERENCES AND NOTES


1. H. Jeffreys, *Geol. Mag.* **79**, 291 (1942).
2. D. P. McKenzie and J. N. Brune, *Geophys. J. R. Astron. Soc.* **29**, 65 (1972).
3. R. H. Sibson, *Nature* **243**, 66 (1973).
4. P. G. Richards, *Bull. Seismol. Soc. Am.* **66**, 1 (1976).
5. M. Kikuchi and H. Kanamori, *Geophys. Res. Lett.* **21**, 2341 (1994).
6. M. Antolik, D. Dreger, B. Romanowicz, *ibid.* **23**, 1589 (1996).
7. S. C. Myers *et al.*, *ibid.* **22**, 2269 (1995).
8. W.-P. Chen, *ibid.*, p. 2261.
9. The value of $D$ is computed from $M_0/\mu S$, where $\mu$ = 1.2 Mbar for the depth of 637 km; $\Delta\sigma$ is computed as $\Delta\sigma = 7\pi\mu D/16r$, for a circular fault with radius $r$ estimated by $r = (S/\pi)^{1/2}$.
10. N. Winslow and L. Ruff, in preparation.
11. *U.S. Geol. Surv. Earthquake Data Report EDR No. 6-94* (1994), p. 145.
12. H. Houston, *Eos* **77**, 491 (1996).
13. T. Hara, K. Kuge, H. Kawakatsu, *Geophys. Res. Lett.* **22**, 2265 (1995).
14. J. Wu, T. Wallace, S. Beck, *ibid.*, p. 2237.
15. H. W. Green and P. C. Burnley, *Nature* **341**, 733 (1989).
16. S. H. Kirby, W. B. Durham, L. A. Stern, *Science* **252**, 216 (1991).
17. P. G. Silver *et al.*, *ibid.* **268**, 69 (1995).
18. E. Orowan, *Geol. Soc. Am. Mem.* **79**, 323 (1960).
19. Here we use "friction" to mean the resistance against fault rupture; it includes the conventional interface friction and the resisting force at the crack tip. In this sense, $\sigma_f$ is the effective frictional stress. The actual energy loss is the sum of interface frictional energy and fracture energy. We assume that these energies will eventually be converted into heat.
20. J. D. Friedman, G. R. Olhoeft, G. R. Johnson, D. Frank, in *The 1980 Eruption of Mount St. Helens, Washington*, P. L. Lipman and D. R. Mullineaux, Eds. (U.S. Geological Survey, Washington, DC, 1981), pp. 557–567.
21. The value of $\Delta T_m$ depends on many parameters, such as the age of subducting slab and the convergence rate. Here we estimate it as 600°C from the category A and B thermal models of S. H. Kirby, S. Stein, A. Okal, and D. C. Rubie [*Rev. Geophys.* **34**, 261 (1996)].
22. The characteristic time scale of local dislocation $\tau_d$ is

estimated from the rise time of the far-field waveforms from the papers used in Table 1. The thermal diffusivity for olivine is taken from C. Clauser and E. Huenges, in *A Handbook of Physical Constants: Mineral Physics and Crystallography*, T. J. Ahrens, Ed. (American Geophysical Union, Washington, DC, 1995), pp. 105–126.
23. B. V. Kostrov, *J. Appl. Math. Mech.* **30**, 1241 (1966).
24. J. D. Eshelby, *J. Mech. Phys. Solids* **17**, 177 (1969).
25. A. J. Rosakis and A. T. Zehnder, *Int. J. Fract.* **27**, 169 (1985).
26. T. Heaton, *Phys. Earth Planet. Inter.* **64**, 1 (1990).
27. Implicit in this assumption is that the frictional loss and surface energy have the same dependence on $V$. If friction does not depend on $V$, then $\eta$ cannot be directly related to $V$.
28. N. F. Mott, *Engineering* **165**, 16 (1948).
29. F. P. Bowden and T. P. Hughes, *Proc. R. Soc. London Ser. A* **172**, 280 (1939).
30. H. Houston and Q. Williams, *Nature* **352**, 520 (1991).
31. M. Furumoto, *Phys. Earth Planet. Inter.* **15**, 1 (1977).
32. D. A. Wiens and J. J. McGuire, *Geophys. Res. Lett.* **22**, 2245 (1995).
33. A. Navrotsky, in *A Handbook of Physical Constants: Mineral Physics and Crystallography*, T. J. Ahrens, Ed. (American Geophysical Union, Washington, DC, 1995), pp. 18–28.
34. P. Lundgren and D. Giardini, *ibid.*, p. 2241.
35. S. Goes and J. Ritsema, *ibid.*, p. 2249.
36. P. F. Ihmle and T. H. Jordan, *ibid.*, p. 2253.
37. S. L. Beck, P. Silver, T. C. Wallace, D. James, *ibid.*, p. 2257.
38. C. H. Estabrook and G. Bock, *ibid.*, p. 2277.
39. We thank J. Rice, A. Rosakis, L. Ruff, H. Houston, and A. Ruben for helpful comments.

30 September 1997; accepted 6 January 1997

# A Determination of the HDO/$H_2O$ Ratio in Comet C/1995 O1 (Hale-Bopp)

Roland Meier,* Tobias C. Owen,* Henry E. Matthews, David C. Jewitt,* Dominique Bockelée-Morvan, Nicolas Biver, Jacques Crovisier, Daniel Gautier

Deuterated water (HDO) was detected in comet C/1995 O1 (Hale-Bopp) with the use of the James Clerk Maxwell Telescope on Mauna Kea, Hawaii. The inferred D/H ratio in Hale-Bopp's water is $(3.3 \pm 0.8) \times 10^{-4}$. This result is consistent with in situ measurements of comet P/Halley and the value found in C/1996 B2 (Hyakutake). This D/H ratio, higher than that in terrestrial water and more than 10 times the value for protosolar $H_2$, implies that comets cannot be the only source for the oceans on Earth.

It is assumed that comets contain unprocessed matter from the earliest history of the solar system. To pursue this subject further, we measured the abundance of HDO in the coma of comet Hale-Bopp using the James Clerk Maxwell Telescope (JCMT) on Mauna Kea. The resulting D/H ratio helps define the processes leading to comet formation and trace the contribution of unmodified ice grains from the original interstellar cloud to various reservoirs of $H_2O$ throughout the solar system.

The HDO ground-state $1_{01}$-$0_{00}$ transition at 464.92452 GHz was detected on 4.9 April 1997 UT (universal time) (Fig. 1), about 5 days after Hale-Bopp passed perihelion (*1*). At the time of the observations, the comet was 0.917 astronomical units (AU) from the sun and 1.385 AU from Earth. We used the C2 single-channel superconductor-isolator-superconductor (SIS) receiver in a double-sideband mode, which convolves the two sidebands into one spectrum. Our setup enabled simultaneous measurement of two high rotational transitions in methanol ($CH_3OH$) and the HDO line without overlap. In the upper sideband, the $CH_3OH$ $9_2$-$9_1$ $A^{\pm}$ transition at 464.835 GHz and the HDO transition yielded line-integrated antenna temperatures $\int T_A dv = 2.37 \pm 0.11$ and $0.64 \pm 0.11$ K km $s^{-1}$, respectively. The $CH_3OH$ $11_2$-$11_1$ $A^{\pm}$ line at 457.006 GHz was detected in the lower sideband and had an integrated line area of $\int T_A dv = 1.71 \pm 0.15$ K km $s^{-1}$ (*2*). At the beginning of the HDO observation, we took a SCUBA image of Hale-Bopp at 850 μm (*3*). Within the typical root-mean-square mechanical stability of the telescope of ±1.5 arc sec, this map allowed us to check our pointing. The stronger of the two $CH_3OH$ lines was then used to monitor our tracking of Hale-Bopp. To achieve continuous sky cancellation, we nodded the secondary mirror at a rate of 1 Hz with a chop throw of 180 arc sec in the azimuthal direction. During its peak-activity, Hale-Bopp was a daytime object, reaching zenith around noon. The solar elongation was 41°. JCMT is the only telescope of its class that is protected against direct solar irradiation with a membrane of woven polytetrafluoroethylene (Gore-Tex), which shades the antenna surface. The membrane transmits over 80% of the incident submillimeter radiation but reflects most of the solar light at shorter wavelengths. We obtained the HDO spectrum during a period of exceptionally dry weather. The zenith opacity at 225 GHz was ≤0.06, which corresponds to a precipitable water column of about 1 mm.

To obtain an accurate D/H ratio in water, one would ideally want to compare HDO with an optically thin line of the rare isotopic molecules $H_2{}^{18}O$ or $H_2{}^{17}O$ using the same telescope; however, all of the stronger transitions of $H_2{}^{18}O$ and $H_2{}^{17}O$ are inaccessible to JCMT. Hence, we compared our observations with production rates measured elsewhere at about the same time. For the first week of April, a water production rate $Q(H_2O) = (1.0 \pm 0.2) \times 10^{31}$ $s^{-1}$ was derived from OH observations at the Nançay radio telescope (*4*). An inspection of the spatial distribution of $H_2O$ (*5*) and ground-based OH data in the near ultraviolet (*6*), however, revealed that derived production rates may depend on aperture size. Follow-up measurements of HDO on 5 April indicated that the absolute calibration of the C2 receiver was not fully reliable at the time of the HDO experiment. As a check, we compared the

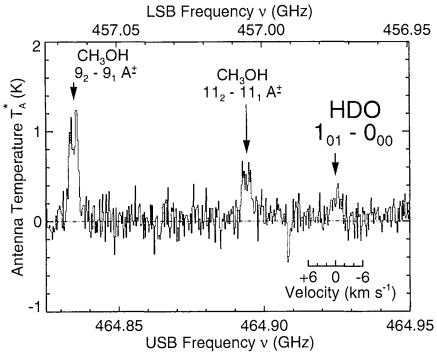


**Fig. 1.** Spectrum of Hale-Bopp showing the HDO $1_{01}$-$0_{00}$ line together with two methanol transitions (120 min, on and off). The $CH_3OH$ $11_2$-$11_1$ $A^{\pm}$ transition originates in the lower sideband (LSB) (top frequency scale); all other lines belong to the upper sideband (USB). Because of different calibrations of the two sidebands, the intensity of the line in the LSB has to be multiplied by a factor of 1.41 (*2*). Each bin covers 313 kHz and is an average of two adjacent channels. Antenna temperatures have been calibrated against internal standards and pointing sources W3(OH) and N7538 IRS1. The velocity scale for the HDO line is relative to the rest frame of the cometary nucleus. The double-peak structure of the lines is caused by the velocity distribution in the comet.

R. Meier, T. C. Owen, D. C. Jewitt, N. Biver, University of Hawaii, Institute for Astronomy, 2680 Woodlawn Drive, Honolulu, HI 96822, USA.
H. E. Matthews, Herzberg Institute for Astrophysics, National Research Council, Victoria, BC V8X 4M6, Canada, and Joint Astronomy Centre, 660 North A'Ohoku Place, Hilo, HI 96720, USA.
D. Bockelée-Morvan, J. Crovisier, D. Gautier, Observatoire de Paris-Meudon, 5 Place Jules Janssen, F-92195 Meudon, Cedex, France.

*Visiting astronomer at the James Clerk Maxwell Telescope, 660 North A'Ohoku Place, Hilo, HI 96720, USA.